Phosphor Materials

DOI: 10.1002/ange.201302494

Nanosegregation and Neighbor-Cation Control of Photoluminescence in Carbidonitridosilicate Phosphors**

Wan-Yu Huang, Fumitaka Yoshimura, Kyota Ueda, Yasuo Shimomura, Hwo-Shuenn Sheu, Ting-Shan Chan, Heather F. Greer, Wuzong Zhou, Shu-Fen Hu, Ru-Shi Liu, and J. Paul Attfield**

Phosphor materials play a key role in white-light emitting diode (LED) devices based on gallium indium nitride (GaInN).[1–5] Phosphors for white LEDs should have good thermal stability and conversion efficiency and an excitation wavelength range in the UV to blue region (370–460 nm).[3,6–8] The yellow-emitting phosphor $(Y,Gd)_3(Al,Ga)_5O_{12}:Ce^{3+}$ is a well-known commercial example, but the lack of red emission results in cold white light and a low color-rendering index (CRI).[1,7,9,10] Nitride-based materials are more covalent than oxides, which improves thermal stability, and their greater crystal field splitting increases the red emission leading to warmer white light.[1,2,11,12] The chemistry of doped nitride phosphors is often complex and it may be difficult to understand how substitutions tune photoluminescence properties, as the local environment of activator ions may be quite different to the structural average. For example, local O/N ordering driven by the size mismatch between the Eu^{2+} activator and the host cations was found to be an important effect in $M_{1.95}Eu_{0.05}Si_{5-x}Al_xO_{8-x}N_x$ (M = Ca, Sr, Ba) phosphors.[12] Herein we demonstrate a new approach to controlling phosphor properties through segregation of activator cations on the nanoscale, as applied to $Sr_{1-x}Y_{0.98+x}Ce_{0.02}Si_4N_{7-x}C_x$ carbidonitridosilicate phosphors, and we show that overall trends evidence a significant neighboring-cation influence.

Two structure types are encountered in the studied system. The $SrYSi_4N_7$ (1147) type structure with hexagonal (space group $P6_3mc$) symmetry contains a network of corner-linked $N(SiN_3)_4$ structural units.[13–16] Sr and Y sites are coordinated by 12 and 6 nitrides, respectively. The related $Y_2Si_4N_6C$ (2461)-type structure has monoclinic $P2_1/c$ symmetry with C substituted only at the 4-connected positions to give $C(SiN_3)_4$ units.[17–19] The 5-coordinate Y1 and 6-coordinate Y2 sites are derived from the Y and Sr sites respectively in the $SrYSi_4N_7$ type. Photoluminescence properties of doped $SrYSi_4N_7$ and $Y_2Si_4N_6C$ types have previously been reported.[14,15,18,19] Eu^{2+}- and Ce^{3+}- doped $SrYSi_4N_7$ respectively emit 548–570 nm yellow light and 450 nm blue light when excited at 390 nm.[14] Photoluminescence of Ce^{3+}- and Tb^{3+}-doped $Y_2Si_4N_6C$ materials,[18] and the underlying Ce^{3+}–Tb^{3+} energy transfer process,[19] have also been investigated, and $Ln_{1.99}Ce_{0.01}Si_4N_6C$ for Ln = Gd and Lu have emission peaks of 610 nm and 540 nm.[19] Several studies have proposed that higher covalence is expected in the $Y_2Si_4N_6C$ network owing to the introduction of carbon, so that the thermal stability of photoluminescence in carbidonitridosilicates is expected to be better than that of corresponding $SrYSi_4N_7$ type nitrides.[17,20,21] However, no studies of the evolution of phosphor properties within $Sr_{1-y}Y_{1+y}Si_4N_{7-y}C_y$ hosts have been reported.

Powder X-ray diffraction (Supporting Information, Figure S1) shows that the $Sr_{1-x}Y_{0.98+x}Ce_{0.02}Si_4N_{7-x}C_x$ samples appear to be solid solutions throughout the $x = 0$–1 range, although more highly resolved synchrotron data reveal a phase-segregated region (see below). Excitation and emission spectra for excitation by 380 nm light are shown in Figure 1a, and the emission positions in the standard CIE chromaticity diagram are indicated on Figure 1b. Both excitation and emission spectra show a substantial red-shift as x increases from 0 to 1. A notable range of useful emissions

[*] W.-Y. Huang, Prof. Dr. R. S. Liu
Department of Chemistry, National Taiwan University
Taipei 106 (Taiwan)
E-mail: rsliu@ntu.edu.tw
F. Yoshimura, Dr. K. Ueda, Dr. Y. Shimomura
Mitsubishi Chemical Group
Science and Technology Research Center, Inc.
Yokohama, Kanagawa 227-8502 (Japan)
Dr. H.-S. Sheu, Dr. T. S. Chan
National Synchrotron Radiation Research Center
Hsinchu 300 (Taiwan)
H. F. Greer, Prof. Dr. W. Zhou
School of Chemistry, University of St Andrews
St Andrews, Fife KY16 9ST (UK)
Prof. Dr. S. F. Hu
Department of Physics, National Taiwan Normal University
Taipei 116 (Taiwan)
Prof. Dr. J. P. Attfield
Centre for Science at Extreme Conditions and School of Chemistry
University of Edinburgh, King's Buildings
Mayfield Road, Edinburgh EH9 3JZ (UK)
E-mail: j.p.attfield@ed.ac.uk

[**] This work was supported by EPSRC, the Leverhulme Trust, and the Royal Society U.K., and the National Science Council of the Republic of China, Taiwan (Contract Nos. NSC 101-2113M-002-014-MY3 and NSC 101-2923M-007-003) and the Mitsubishi Chemical Group, Science and Technology Research Center, Inc. We are grateful to Chia-Han Chen for assistance in fitting data and preparing figures, and Tsung-Han Lin for providing an ultrafast personal computer in this work.

Supporting information for this article is available on the WWW under http://dx.doi.org/10.1002/anie.201302494.

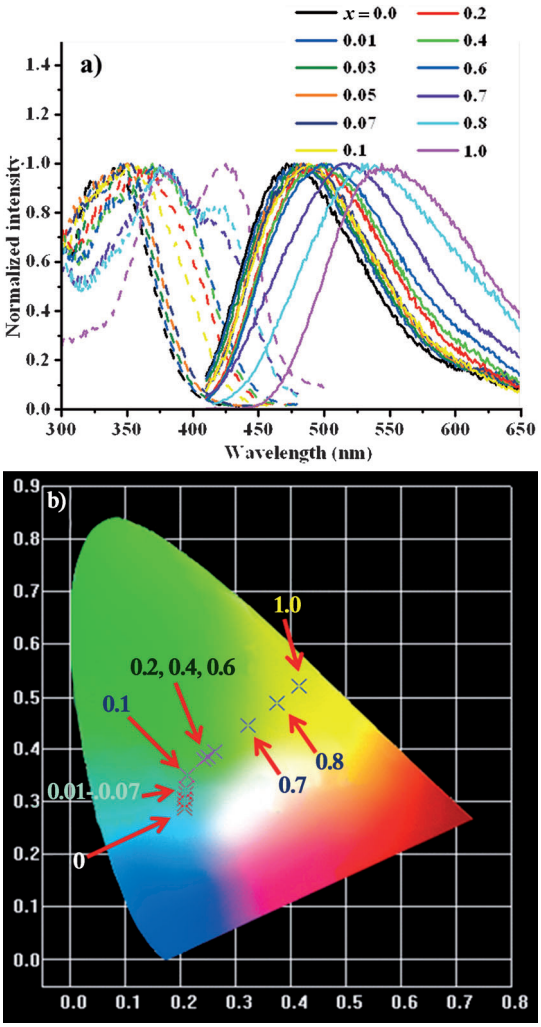

Figure 1. a) Excitation (-----) and emission (——) spectra and b) CIE chromaticity positions for $Sr_{1-x}Y_{0.98+x}Ce_{0.02}Si_4N_{7-x}C_x$ samples.

is observed; blue for $x = 0$–0.07, blue–green for $x = 0.1$, green for $x = 0.2$–0.6, yellow–green for $x = 0.7$ and yellow for $x = 0.8$ and 1.0 samples. Thus, the $x \geq 0.1$ emissions can be stimulated by near-UV or blue light from an LED, so these materials may be useful white-LED phosphors.

Thermal quenching of photoluminescence is undesirable for applications, so the variations of peak emission intensity I_T were measured from ambient temperature up to 573 K (Figure 2a). These are fitted as $I_T/I_0 = [1 + D\exp(-E_a/kT)]^{-1}$, where I_0 (intensity at $T = 0$), D, and the activation energy for thermal quenching E_a were refined variables. A systematic decrease of activation energy is observed in the $Sr_{1-x}Y_{0.98+x}Ce_{0.02}Si_4N_{7-x}C_x$ system as x increases. The blue-emitting $x = 0$ material has the largest activation barrier for quenching, and is 100% efficient (compared to $T = 0$ emission) at 300 K. The green-emitting $x = 0.1$–0.6 materials have very similar activation energies and 90% relative efficiency at room temperature. The yellow–green $x = 0.7$ phosphor has 75% efficiency and yellow $x = 0.8$ and 1.0 phosphors have the smallest activation energies and are 60% efficient at 300 K.

The overall trends in emission wavelength and thermal quenching energy in the $Sr_{1-x}Y_{0.98+x}Ce_{0.02}Si_4N_{7-x}C_x$ system are

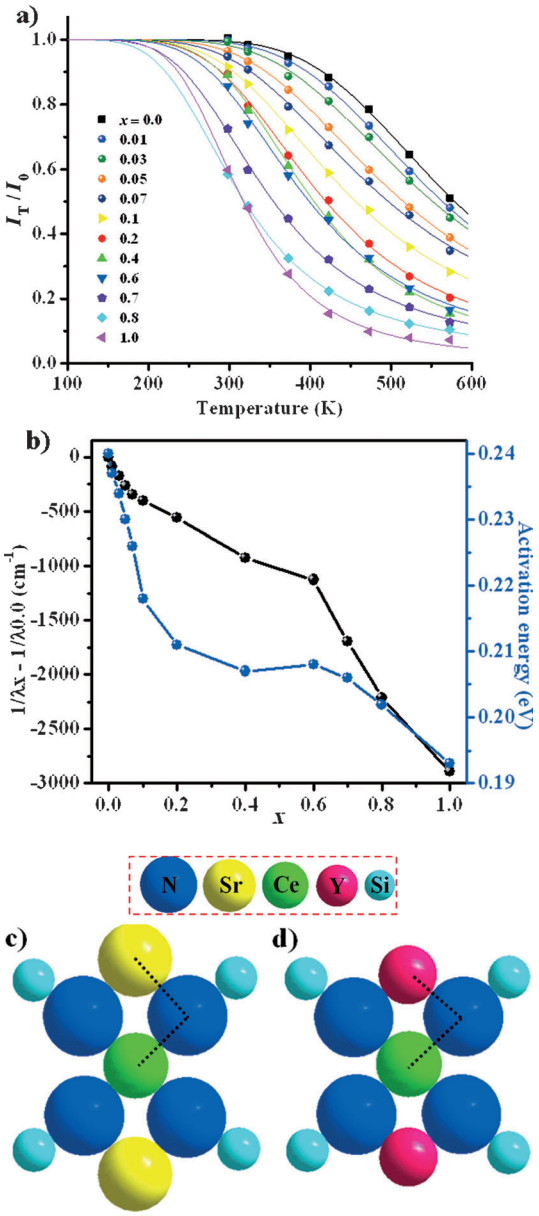

Figure 2. a) Temperature dependence of the peak emission intensity, normalized to $T = 0$ values, and b) shifts of the peak emission energy [cm^{-1}] as inverse wavelength, and thermal activation energy [eV] from fits shown in (a), with x in $Sr_{1-x}Y_{0.98+x}Ce_{0.02}Si_4N_{7-x}C_x$ phosphors. Representation of the local first- and second-coordination around Ce^{3+} activator ions occupying Y^{3+} sites in $Sr_{1-x}Y_{0.98+x}Ce_{0.02}Si_4N_{7-x}C_x$ phosphors for c) $x = 0$ and d) $x = 1$.

shown in Figure 2b. The overall trend of decreasing quenching activation energy with increasing x is surprising, as the progressive replacement of Sr^{2+} and N^{3-} by Y^{3+} and C^{4-} was expected to introduce more covalency into the materials and hence raise lattice rigidity and the quenching barrier height.[21,22] We propose that this reveals a dominant neighboring-cation influence as follows.

Ce^{3+} cations are coordinated by first-neighbor nitrides that are also connected to other cations through linking of coordination polyhedra, as well as Si atoms. As x increases, larger Sr^{2+} (1.18 Å) is substituted by smaller Y^{3+} (0.90 Å) at

second-neighbor sites to Ce^{3+} cations,[22] while further N^{3-} (connected only to four silicon atoms) is replaced by C^{4-}. Thus the Sr^{2+}/Y^{3+} substitution in the second coordination sphere[23] has a strong effect at Ce^{3+} activator sites. The local structures around Ce^{3+} activator ions occupying Y^{3+} sites in the $x=0$ and $x=1$ materials are shown in Figure 2c and d, respectively. The degree of covalency in the Ce–N bonding is controlled by the bonding of the nitride to other neighbors (essentially a competition between Ce^{3+} and the neighboring cations for the nitride electron density). Sr^{2+} ions form relatively ionic bonds to nitride, so Ce–N covalency is enhanced, whereas Y–N bonds are more covalent, so Ce–N covalency is reduced. Thus the Ce–N bonds become less covalent as the second-neighbor Sr^{2+} cations around Ce^{3+} are replaced by Y^{3+} with increasing x. This neighboring-cation influence progressively decreases the quenching activation energy as the Ce–N bonds become less covalent.

The increasing red-shift with x in $Sr_{1-x}Y_{0.98+x}Ce_{0.02}Si_4N_{7-x}C_x$ appears anomalous given the above covalency arguments. However, similar shifts are observed in some other nitrides, for example from 586 nm peak emission for $Ba_2Si_5N_8$:Eu^{2+} to 630 nm for isostructural $Sr_2Si_5N_8$:Eu^{2+}.[24] Here the neighboring-cation influence of replacing Ba^{2+} by Sr^{2+} is outweighed by the overall effect of the lattice contraction, leading to a red-shift of emission, and the same argument may apply to the $Sr_{1-x}Y_{0.98+x}Ce_{0.02}Si_4N_{7-x}C_x$ system given the general decrease of lattice volume with x shown in Figure 3.

Irregularities in the variations of thermal quenching energy in Figure 2 reveal important structural and microstructural effects on the activator cation distribution in the $Sr_{1-x}Y_{0.98+x}Ce_{0.02}Si_4N_{7-x}C_x$ system. The $x=0.2$–0.6 samples have a near-constant green emission that does not follow the general trend of photoluminescence and thermal quenching energy in Figures 1 and 2. This shows microstructural effects, which were investigated through synchrotron X-ray diffraction (SXRD), EXAFS, and electron microscopy studies. Rietveld fits to SXRD data showed that $x=0$ and $x=1$ samples are single-phase hexagonal (H) 1147 and monoclinic (M) 2461 types, respectively (for lattice constants and plots, see the Supporting Information, Table S1 and Figure S2). However, analysis of $x=0.2$–0.6 samples revealed the presence of both 1147 and 2461-type phases, as shown for the $x=0.2$ material in Figure 3a. No significant coexistence was found for $x=0.8$, where the fraction of 1147 phase refined to less than 1%. These results demonstrate that the structural transformation from hexagonal to monoclinic symmetry starts near $x=0.1$, as shown by the discontinuity on the CIE chromaticity diagram in Figure 1b, and proceeds through a broad two-phase region that ends at $x\approx0.7$. The monoclinic (M) 2461-type has a volume-doubled supercell of the hexagonal (H) 1147-type, and their lattice parameters are related as $a_M\approx c_M/2\approx a_H$; $b_M\approx c_H$; $\beta_M\approx\gamma_H$ ($=120°$). The variations of the phase fractions and related lattice parameters with x are shown in Figure 3b. The parameters for each phase evolve smoothly, and the lattice volumes decrease with increasing x, as the substitution of large Sr^{2+} by small Y^{3+} is the dominant effect. However, it is notable that the volumes of the 1147 and 2461 components in the $x=0.2$ and 0.4 samples differ significantly, suggesting that cations are segregated between them.

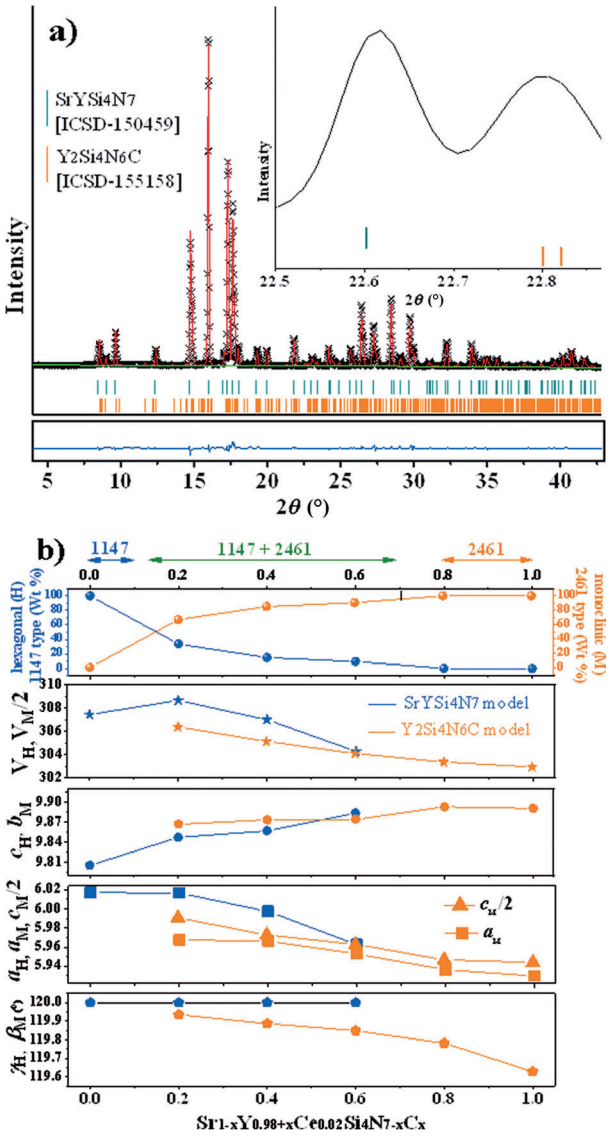

Figure 3. a) Rietveld fit to SXRD data for the $x=0.2$ sample, with an expanded region inset to demonstrate the presence of both 1147 and 2461 type phases. b) Variations of the weight (or molar) percentages and cell axis lengths [Å] and volumes [Å^3] for hexagonal (H) 1147-type and monoclinic (M) 2461-type phases with x in the $Sr_{1-x}Y_{0.98+x}Ce_{0.02}Si_4N_{7-x}C_x$ samples.

The likely segregation of larger cations (Sr^{2+} and Ce^{3+}) to the 1147 phase (with excess N for charge compensation), while the smaller-volume 2461 phase will be more Y^{3+} (and C)-rich. This is consistent with the photoluminescence properties noted above, as the two-phase $x=0.2$, 0.4, and 0.6 samples have very similar green emissions and the energy shift for $x=0.2$–0.6 in Figure 2b does not follow the average trend. Thus, the green emission is assigned to the hexagonal 1147-type component in the two-phase $x=0.2$–0.6 materials. This is corroborated by the emergence of a new excitation band at 420 nm for $x\geq0.7$ samples in Figure 1a. The SXRD patterns of $x=0.8$ and 1.0 samples contain only the 2461 $Y_2Si_4N_6C$-type phase, in which Ce^{3+} has a yellow emission.

Y K-edge EXAFS spectra were used to investigate changes in local structure across the $Sr_{1-x}Y_{0.98+x}Ce_{0.02}Si_4N_{7-x}C_x$ series (see the Supporting Information, Figure S4). A single broad envelope is observed for the nearest-neighbor Y–N distances. Changes in this with x reflect the presence of two distinct sites in the $x=1$ end-member, but the EXAFS results are not sensitive to the phase separation observed in the $x=$ 0.2–0.6 region.

Microstructures of three $Sr_{1-x}Y_{0.98+x}Ce_{0.02}Si_4N_{7-x}C_x$ samples were examined using HRTEM. Typical HRTEM images from the $x=0$ and $x=1$ materials (Figure 4a,b) show a very uniform contrast, indicating that these single-phase samples

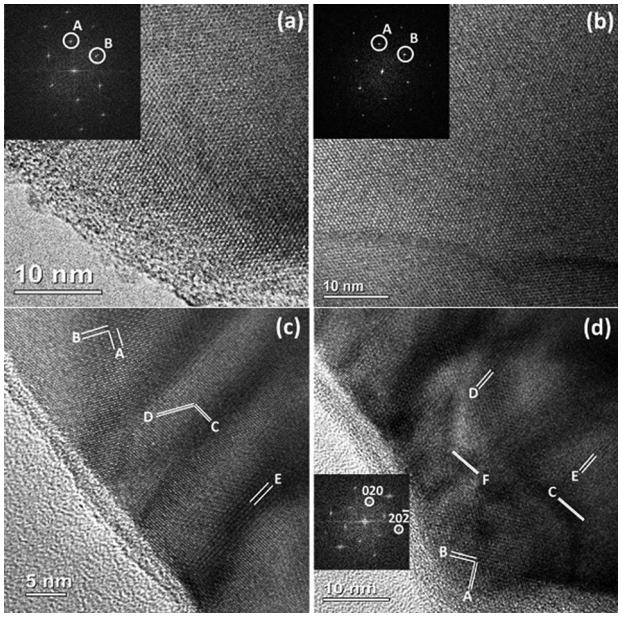

Figure 4. HRTEM images of $Sr_{1-x}Y_{0.98+x}Ce_{0.02}Si_4N_{7-x}C_x$ samples. a) [10$\bar{1}$] zone image of the hexagonal 1147 type $x=0$ sample; diffraction points A and B in the inset FFT (Fast Fourier Transform) pattern have d-spacings of 4.65 and 5.19 Å, corresponding to the (101) and (010) planes. b) [0$\bar{1}$0] zone image of the monoclinic 2461 type $x=1$ sample; A and B have $d=5.16$ and 5.11 Å, indexed as (100) and (10$\bar{2}$). c) and d) show multidomain nanostructures in the two-phase $x=0.4$ sample. The identified planes A–E in (c) have d-spacings 9.93, 6.00, 3.00, 2.94 and 5.19 Å; respectively indexed as $(010)_M$, $(10\bar{1})_M$, $(110)_H$, $(1\bar{2}0)_H$, and $(002)_M$, where H and M subscripts refer to the hexagonal 1147 type and monoclinic 2461 type lattices. Planes A–F in (d) have $d=2.95$, 5.07, 2.82, 5.16, 4.91, and 2.83 Å corresponding to $(20\bar{2})_M$, $(020)_M$, $(103)_H$, $(100)_M$, $(020)_M$, and $(103)_H$. The FFT inset is of the lower domain in (d).

are highly crystalline and without significant defects. However, micrographs from the biphasic $x=0.4$ sample reveal complex multidomain nanostructures (Figure 4c,d). The domains have dimensions in the range of 5–15 nm. Although the lattices of the hexagonal 1147 and monoclinic 2461 phases are closely related, images displaying large d-spacings may be used to distinguish between them. Three domains have been identified in the platy microstructure of Figure 4c. d-spacings measured from the crystal fringes marked A and B identify the upper domain as 2461 phase, whilst d-spacings calculated from the fringes marked C and D in the adjacent domain correspond to the hexagonal 1147 phase, and the lower domain with crystal fringes marked E matches to the 2461 type phase. Therefore, the platy microstructure results from intergrowths of alternating 1147 and 2461 type lamellae. In the irregular microstructure shown in Figure 4d, the lower domain containing lattice fringes marked A and B is identified as the 2461-type phase, whereas adjacent regions (of planes C and F) are 1147-type, and D and E are from 2461-type domains. An alternation of 1147 and 2461-type domains is again apparent. Electron microscopy thus enables the length scale for the cation segregation evidenced from photoluminescence properties to be identified as the 5–15 nm domain size of the observed intergrowths of 1147 and 2461 phases. Thus the $x=0.2$–0.6 $Sr_{1-x}Y_{0.98+x}Ce_{0.02}Si_4N_{7-x}C_x$ materials are nanosegregated phosphors, where the phase separation into hexagonal 1147 and monoclinic 2461 type domains and the accumulation of Ce^{3+} activators in the 1147 phase leads to a useful green emission that varies little with x, and has a high (90%) relative thermal efficiency at room temperature.

The above results underline the importance of controlling the local environment of the activator cations in nitride phosphors. The overall trends in the $Sr_{1-x}Y_{0.98+x}Ce_{0.02}Si_4N_{7-x}C_x$ system are strongly influenced by neighboring-cation effects. Low thermal quenching rates at room temperature are assisted by high covalency in the activator-nitride bonding, and this is enhanced when neighboring cations have relatively low charges (+1 or +2), thus the good performances of doped $M_2Si_5N_8$ and $MSi_2O_2N_2$ (M = Ca, Sr, Ba), and MSi_6N_8 (M = Sr, Ba) materials. A new aspect of chemical control is illustrated by the discovery of useful green emission from the two-phase $x=0.2$–0.6 materials, where the Ce^{3+} activator environment results from nanoscale cation segregation.

As a further examination of the utility of these materials, water resistance tests were also performed (Supporting Information, Figure S5). The conductivities of dispersions of green ($x=0.2$, 0.4, and 0.6) $Sr_{1-x}Y_{0.98+x}Ce_{0.02}Si_4N_{7-x}C_x$ phosphors dispersed in deionized water are comparable to that of the green commercial phosphor $BaMg_2Al_{16}O_{27}:Eu^{2+},Mn^{2+}$ and far below that of $(Ba,Sr)_2SiO_4:Eu^{2+}$, and all of the $Sr_{1-x}Y_{0.98+x}Ce_{0.02}Si_4N_{7-x}C_x$ materials show excellent water resistance.

In summary, the $Sr_{1-x}Y_{0.98+x}Ce_{0.02}Si_4N_{7-x}C_x$ system is notable as blue, green, and yellow phosphors are obtained as x increases from 0 to 1. The overall decreases in quenching barrier height result from a neighboring-cation effect, through which the replacement of Sr^{2+} neighbors by Y^{3+} reduces the covalency of Ce–N bonding. Green emission results from nanosegregation of cations between hexagonal $SrYSi_4N_7$ type and monoclinic $Y_2Si_4N_6C$ type components in two-phase $x=0.2$–0.6 samples, and demonstrates the importance of nanostructural as well as lattice control of phosphor properties. Such nanosegregation at immiscibility gaps between host structure types may enable photoluminescence to be shifted into useful new wavelength regions in other phosphors.

Experimental Section

Ceramic 1.0 g samples of $Sr_{1-x}Y_{0.98+x}Ce_{0.02}Si_4N_{7-x}C_x$ (x = 0.0, 0.01, 0.03, 0.05, 0.07, 0.1, 0.2, 0.4, 0.6, 0.7, 0.8, and 1.0) were synthesized by the solid-state reaction from stoichiometric mixtures of high purity Sr_3N_2 (Kojundo, 99.0%), YN (Kojundo, 99.0%), α-Si_3N_4 (Kojundo, 99.0%), CeN (Cerac, 99.9%), and SiC (ACROS, 99.0%). Precursors were ground and mixed in an agate mortar in a glove box, where concentrations of moisture and oxygen were less than 1 ppm. The powders were placed in a BN crucible (for $x = 0.0$) or graphite crucibles (for $x = 0.01$–1.0 samples) and fired using a graphite heater in a gas-pressure sintering furnace (FVPHP-R-5, FRET-25, Fujidempa Kogyo Co. Ltd.). The temperature was raised to 800 °C under a vacuum of 10^{-2} Pa and then held for 40 min, then nitrogen gas (99.999% purity) was introduced at a pressure of 0.92 MPa, and the temperature was increased to 1950 °C and held at that value for 2 h. The sintered products were slow cooled to room temperature.

All of the measurements and analysis were performed on finely ground powders. Samples were analyzed by X-ray diffraction (XRD) using a D2 Phaser diffractometer (Bruker) with Cu Kα radiation. Synchrotron X-ray diffraction (SXRD) patterns for $x = 0$, 0.2, 0.4, 0.6, 0.8, and 1.0 samples were recorded at the BL01C2 beamline of the National Synchrotron Radiation Research Center (NSRRC), Taiwan, equipped with a Mar345 imaging plate and using an X-ray wavelength of 0.77491 Å. X-ray Rietveld refinements were conducted using the GSAS (General Structure Analysis System) software.[25] Y K-edge extended X-ray absorption fine structure (EXAFS) spectra were recorded at BL01C1 of the NSRRC. High resolution transmission electron microscopic (HRTEM) images were obtained on a JEOL JEM-2011 microscope operated at 200 kV. Photoluminescence spectra were measured using a FluoroMax-3 spectrophotometer equipped with a 150 W Xe lamp and a Hamamatsu R928 photomultiplier tube, and a heater (THMS-600) for temperature-dependent spectra.

Received: March 25, 2013
Revised: May 17, 2013
Published online: June 21, 2013

Keywords: carbidonitridosilicate · phosphors · photoluminescence · thermal quenching

[1] H. A. Höppe, *Angew. Chem.* **2009**, *121*, 3626; *Angew. Chem. Int. Ed.* **2009**, *48*, 3572.
[2] C. W. Yeh, W. T. Chen, R. S. Liu, S. F. Hu, H. S. Sheu, J. M. Chen, H. T. Hintzen, *J. Am. Chem. Soc.* **2012**, *134*, 14108.
[3] Y. Q. Li, N. Hirosaki, R.-J. Xie, T. Takeda, M. Mitomo, *Chem. Mater.* **2008**, *20*, 6704.
[4] R. Wang, J. Zhang, X. Xu, Y. Wang, L. Zhou, B. Li, *Mater. Lett.* **2012**, *84*, 24.
[5] C. Wickleder, *Angew. Chem.* **2011**, *123*, 832; *Angew. Chem. Int. Ed.* **2011**, *50*, 806.
[6] J. H. Oh, J. R. Oh, H. K. Park, Y.-G. Sung, Y. R. Do, *Opt, Express* **2011**, *19*, A270.
[7] C. H. Huang, T. M. Chen, *Inorg. Chem.* **2011**, *50*, 5725.
[8] O. M. ten Kate, Z. Zhang, P. Dorenbos, H. T. Hintzen, E. van der Kolk, *J. Solid State Chem.* **2013**, *197*, 209.
[9] M. Roushan, X. Zhang, J. Li, *Angew. Chem.* **2012**, *124*, 451; *Angew. Chem. Int. Ed.* **2012**, *51*, 436.
[10] J.-S. Shin, H.-J. Kim, Y.-K. Jeong, K.-B. Kim, J.-G. Kang, *Mater. Chem. Phys.* **2011**, *126*, 591.
[11] M. Zeuner, S. Pagano, W. Schnick, *Angew. Chem.* **2011**, *123*, 7898; *Angew. Chem. Int. Ed.* **2011**, *50*, 7754.
[12] W. T. Chen, H. S. Sheu, R. S. Liu, J. P. Attfield, *J. Am. Chem. Soc.* **2012**, *134*, 8022.
[13] C. M. Fang, Y. Q. Li, H. T. Hintzen, G. de With, *J. Mater. Chem.* **2003**, *13*, 1480.
[14] Y. Q. Li, C. M. Fang, G. de With, H. T. Hintzen, *J. Solid State Chem.* **2004**, *177*, 4687.
[15] R.-J. Xie, N. Hirosaki, *Sci. Technol. Adv. Mater.* **2007**, *8*, 588.
[16] D. P. Thompson, Y. Zhang, *Key Eng. Mater.* **2009**, *403*, 3.
[17] K. Liddell, D. P. Thompson, S. J. Teat, *J. Eur. Ceram. Soc.* **2005**, *25*, 49.
[18] H. Zhang, T. Horikawa, K.-I. Machida, *J. Electrochem. Soc.* **2006**, *153*, H151.
[19] C. Duan, Z. Zhang, S. Rösler, S. Rösler, A. Delsing, J. Zhao, H. T. Hintzen, *Chem. Mater.* **2011**, *23*, 1851.
[20] H. A. Höppe, G. Kotzyba, R. Pöttgen, W. Schnick, *J. Mater. Chem.* **2001**, *11*, 3300.
[21] K. Liddell, D. P. Thompson, T. Bräuniger, R. K. Harris, *J. Eur. Ceram. Soc.* **2005**, *25*, 37.
[22] R. D. Shannon, *Acta Crystallogr. Sect. A* **1976**, *32*, 751.
[23] G. Blasse, N. Sabbatini, *J. Solid State Chem.* **1987**, *70*, 93.
[24] Y. Q. Li, J. E. J. van Steen, J. W. H. van Krevel, G. Botty, A. C. A. Delsing, F. J. DiSalvo, G. de Witha, H. T. Hintzen, *J. Alloys Compd.* **2006**, *417*, 273.
[25] A. C. Larson, R. B. Von Dreele, "General Structure Analysis System (GSAS)", Los Alamos National Laboratory Report LAUR 86–748, **2000**.